Hindawi
International Journal of Aerospace Engineering
Volume 2022, Article ID 9024739, 17 pages
https://doi.org/10.1155/2022/9024739

Research Article

Dynamic Characteristics Analysis of 3D Blade Tip Clearance for Turbine Blades with Typical Cracks

Xiaodong Zhang[1,2] **Yiwei Xiong**[1] **Xin Huang**[1] **Bochao Fan**[1] **Zhen Zhao**[1,3] **and Jiahao Zhu**[1]

[1]*School of Mechanical Engineering, Xi'an Jiaotong University, No. 28, Xianning West Road, Xi'an 710049, China*
[2]*Key Laboratory of Education Ministry for Modern Design and Rotor-Bearing System, Xi'an Jiaotong University, No. 28, Xianning West Road, Xi'an 710049, China*
[3]*CRRC Zhuzhou Electric Co., Ltd., Zhuzhou 412000, China*

Correspondence should be addressed to Yiwei Xiong; beiweilife@163.com

Received 5 June 2022; Revised 3 August 2022; Accepted 12 August 2022; Published 6 September 2022

Academic Editor: Chuang Liu

As well known, the crack is a typical fault of turbine blades, which is difficult to detect due to the weak fault features contained in the rotor vibration. Although some fault diagnosis methods based on blade tip timing (BTT) are proposed to detect blade cracks, the limited fault features can be extracted because the BTT signals contain only one-dimensional fault information. Based on the dynamic analysis, the cracked blade undergoes three-dimensional (3D) deformation so that it would be reflected in the changes of the three-dimensional blade tip clearance (3D-BTC). Therefore, the dynamic characteristics of the 3D-BTC of turbine blades with typical cracks should be investigated to obtain its change rule and achieve a more comprehensive diagnosis of blade cracks. In this paper, the 3D finite element model of the turbine blisk is established, and the fluid-thermal-solid coupling analysis is implemented to calculate the blade deformation. Then, a novel dynamic computation method is proposed to calculate the 3D-BTC based on the blade deformation. The typical blade cracks are taken into consideration, and the dynamic characteristics of the 3D-BTC regarding the typical cracks are analyzed to obtain its change rule. The results show that abundant crack fault information can be obtained based on the 3D-BTC, which can facilitate the comprehensive diagnosis of turbine blade cracks.

1. Introduction

The turbine blade failures frequently occur due to the extremely harsh working environment of aeroengines, and the crack fault is particularly prominent for turbine blades, which seriously affects the safety and reliability of aeroengines. Thus, it is of great significance to monitor and diagnose the crack fault of turbine blades. However, the conventional diagnosis method based on the vibration signals of the rotor has difficulty detecting blade cracks due to the high complexity of the coupled vibration of the turbine rotor system [1]. Thus, the weak fault features of the crack are prone to be overwhelmed by noise and hard to be extracted from the vibration signals. Therefore, some more effective monitoring methods for blade cracks are greatly demanded.

Nowadays, some noncontact measurement methods for blade vibration are proposed, and the blade tip timing (BTT) technology attracts wide attention [2]. Some basic methods based on the BTT, such as the single-parameter method and two-parameter plot, were proposed to extract the vibration frequency of blades [3, 4]. In addition, the compressed sensing theory and sparse representation method were also combined with the BTT to analyze the multifrequency vibration of blades [5, 6]. However, the BTT signal is severely undersampled, and complicated signal processing methods are required to analyze the blade vibration frequency [7]. Except for measuring the blade vibration, scholars established some dynamic models to analyze the vibration characteristics theoretically. Xu et al. proposed a novel dynamic model and a thermoelastic model for a

hemispherical shell resonator with thickness nonuniformity and clarified the effect of thickness nonuniformity and thermal deformations on the output error of the hemispherical shell resonator [8, 9]. In order to analyze the blade vibration response, Xie et al. established a dynamic model of a rotating twisted shrouded blade based on Timoshenko beam theory [10], and Oh and Yoo proposed a dynamic model for a rotating blade with an arbitrary cross-section [11]. Actually, the crack will lead to the deformation of the blade in three-dimensional (3D) space under complicated loads, and the crack fault information should have 3D characteristics. However, the blade vibration or the BTT signals only contain one-dimensional (circumferential vibration) information. Thus, the fault features extracted from the blade vibrations cannot fully reflect the crack fault information of turbine blades.

The blade tip clearance (BTC) is a core parameter of the aeroengine, and the dynamic characteristics of BTC can reflect the working conditions and fault information of turbine blades [12]. Thus, the information of blade cracks can be reflected in the change of the BTC, so it is crucial to understand the dynamic characteristics and the change rule of the BTC. Kypuros and Melcher and Agarwal et al. established a reduced model of BTC by considering the radial deformation of the turbine disk, blade, and casing so that the estimation of the BTC was close to the measurement results [13, 14]. Chapman et al. used a first-principle approach to estimate the thermal and mechanical deformations of the turbine and presented a generic but realistic BTC model of the high-pressure turbine [15]. Jia et al. investigated the effects of rotor crack and rotor vibration on the change rule of high-pressure turbine BTC based on a reduced model [16, 17]. Moreover, Ju utilized the finite element method (FEM) to analyze the radial deformation of the turbine blade, disk, and casing, and the change rules of BTC were further obtained [18]. However, the aforementioned researches only focus on the change of radial BTC, which contains only one-dimensional fault information. Hence, the fault features extracted from the radial BTC are also insufficient.

To overcome the deficiencies that the BTT signal and the conventional BTC cannot fully reflect the fault information of blade cracks, Teng et al. proposed the three-dimensional blade tip clearance (3D-BTC), which contains comprehensive crack fault information in three dimensions [19]. Moreover, in order to realize the fault diagnosis of blade cracks based on the 3D-BTC, an optical fiber sensor with three sensing units was designed to monitor the 3D-BTC [20]. Besides, the 3D-BTC demodulation method was proposed, and a dynamic measurement system was established so that the 3D-BTC could be accurately measured [21–23]. In addition, the change rules of the 3D-BTC of normal and cracked blades were studied utilizing the FEM, and the nickel-based superalloy GH4169 was used as the blade material [24], which also can be used in the field of aerospace engineering, such as the electromagnetic docking system due to its good mechanical properties [25, 26]. The effects of through-thickness crack on the 3D-BTC were analyzed [19, 24], which indicates that the 3D-BTC contained abundant fault information on the blade cracks.

The change rule of 3D-BTC has been investigated in the previous studies [19, 24], but there are still some deficiencies that need to be improved. First, the computation method of 3D-BTC is unreasonable in the previous studies. The 3D-BTC refers to the spatial distance between the blade tip surface and the casing inner surface, so it is more reasonable to select the points on the casing inner surface as the reference points to calculate the 3D-BTC. However, the reference points are on the blade tip surface in the previous studies. Second, only the through-thickness cracks at the blade trailing edge are investigated in the previous studies. However, the surface crack is also typical for turbine blades in practice, and it may appear in different positions of the blade, such as the leading edge, trailing edge, pressure side, and suction side [27]. Kianicova and Pokluda performed the fractographic analysis on several turbine blades and pointed out that the typical surface cracks were initiated from the middle of the blade body close to the trailing edge [28], and the surface crack at the blade trailing edge will propagate due to the cycle load [29]. Besides, cracks may appear on the leading edge of the blade due to the impact of high-temperature and high-pressure gas [30]. Mokaberi et al. revealed that the crack also initiated from the corrosion pit on the blade leading edge according to the microstructural features of the blade [31]. Moreover, the surface crack may also appear on the pressure side and the suction side of the turbine blades due to some factors such as high-/low-cycle fatigue, manufacturing flaws, and stress corrosion [32–34].

To address the above problems, at first, a novel dynamic computation method of 3D-BTC is proposed based on the reference points on the casing inner surface and the blade deformation obtained from the FEM. Then, the typical cracks, including the through-thickness crack and the surface crack, on the leading edge, trailing edge, pressure side, and suction side of the blade are considered in this paper. Lastly, the stress field near the crack front and the effects of crack size and position on the dynamic characteristics of the 3D-BTC are investigated. Compared with the conventional BTC, the 3D-BTC provides abundant fault information on the typical crack of the blade, which provides a theoretical basis for the fault feature extraction of blade typical cracks.

The rest of this paper is organized as follows. In Section 2, the FE analysis method for the turbine blade is briefly introduced, and a novel dynamic computation method for the 3D-BTC is proposed. The three-dimensional FE model of the turbine blisk is introduced in Section 3, and both the through-thickness crack and the surface crack are considered in this model. In Section 4, the stress field near the crack is analyzed, the 3D-BTC of turbine blades with typical cracks are obtained, and the effects of typical cracks on the 3D-BTC dynamic characteristics are analyzed. The results indicate that the 3D-BTC is more sensitive to the blade typical crack than the conventional RTC, so more valuable blade crack fault information can be obtained based on the 3D-BTC. Finally, some conclusions are given in Section 5.

2. Dynamic Computation Method for the 3D-BTC of Turbine Blade

2.1. The 3D Blade Tip Clearance. The turbine blade usually has a twist shape and undergoes complicated deformation due to the working loads and the blade crack, which leads

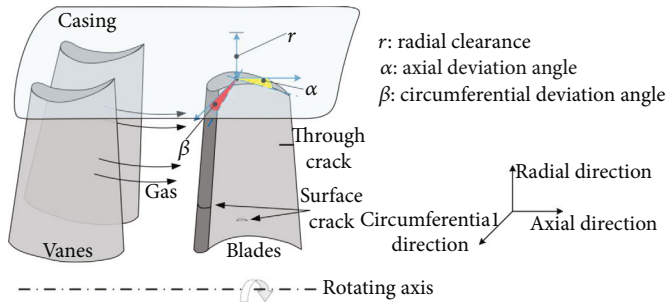

Figure 1: Description of the 3D-BTC.

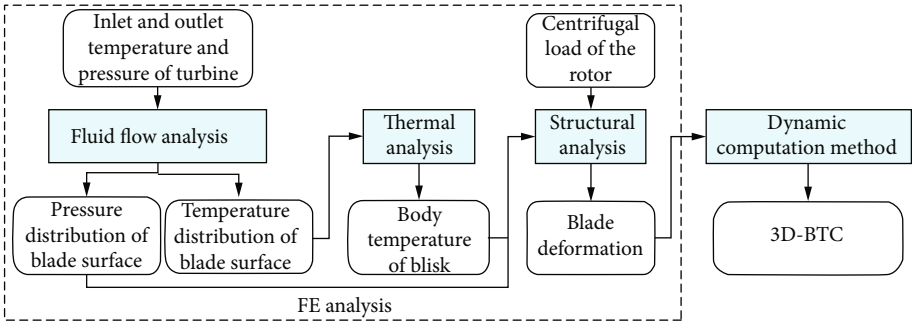

Figure 2: The flowchart for analyzing the 3D-BTC of turbine blades.

to the BTC presenting 3D features. Thus, the 3D-BTC is proposed to characterize the 3D deformation of turbine blades [19], as shown in Figure 1. It consists of radial tip clearance (RTC), axial deflection angle (ADA), and circumferential deflection angle (CDA), which can fully reflect the 3D spatial characteristics between the blade tip and the casing inner surface.

The 3D-BTC is mainly affected by the thermal load and aerodynamic load caused by the high-temperature and high-pressure gas and the centrifugal load caused by the high rotating speed of the rotor. Therefore, these factors need to be considered when analyzing the 3D-BTC dynamic characteristics, and the analyzing flowchart for the 3D-BTC of turbine blades is shown in Figure 2.

2.2. The FE Analysis for the Turbine Blades. According to the flowchart shown in Figure 2, the fluid-thermal-solid sequential coupling analysis is implemented to obtain the deformation of turbine blades. First of all, it is essential to perform the fluid flow analysis so that the temperature distribution and pressure distribution of the blade surface can be obtained. Thus, the commercial computational fluid dynamics software CFX is used to solve the continuity equation, momentum equation, and energy equation of the fluid around the turbine blade, which can be expressed as [35]

$$\frac{\partial \rho}{\partial t} + \nabla \cdot (\rho \mathbf{U}) = 0, \tag{1}$$

$$\frac{\partial (\rho \mathbf{U})}{\partial t} + \nabla \cdot (\rho \mathbf{U} \otimes \mathbf{U}) = -\nabla p + \nabla \cdot \tau + \mathbf{S}_M, \tag{2}$$

$$\frac{\partial (\rho E)}{\partial t} + \nabla \cdot [\mathbf{U}(\rho E + p)] = \nabla \cdot \left[k_{\text{eff}} \nabla T - \sum_j h_j J_j + (\tau_{\text{eff}} \cdot \mathbf{U}) \right] + \mathbf{S}_h. \tag{3}$$

Here, $\mathbf{U}$ is the velocity vector of the fluid, ρ is the fluid's density, and p is the fluid's pressure. The ∇ refers to the Hamiltonian operator. In Equations (2) and (3), E is the total energy, k_{eff} is the effective thermal conductivity, h_j is the enthalpy, J_j is the diffusion flux, and $\mathbf{S}_M$ and $\mathbf{S}_h$ are the heat source and momentum source, respectively. Moreover, τ is the viscous stress tensor, expressed as

$$\tau = \mu \left[\nabla \mathbf{U} + (\nabla \mathbf{U})^T - \frac{2}{3} \delta \nabla \cdot \mathbf{U} \right]. \tag{4}$$

Here, μ is the dynamic viscosity, and δ is the unit tensor. In addition, the shear stress transport (SST) turbulence model is used, which combines the advantages of the $k-\omega$ model and $k-\varepsilon$ model. The SST model accounts for the transport of the turbulent shear stress so that the eddy viscosity will not be overpredicted. Thus, it is more suitable for the turbulence simulation in this paper. The SST model can be expressed as Equations (5) and (6), and in Equation (6), v_t is the eddy viscosity, which can be expressed as [36]

$$\frac{\partial (\rho k)}{\partial t} + \nabla \cdot (\rho \mathbf{U} k) = \nabla \cdot \left[\left(\mu + \frac{\mu_t}{\sigma_{k3}} \right) \nabla k \right] + \overline{P_k} - \beta' \rho k \omega, \tag{5}$$

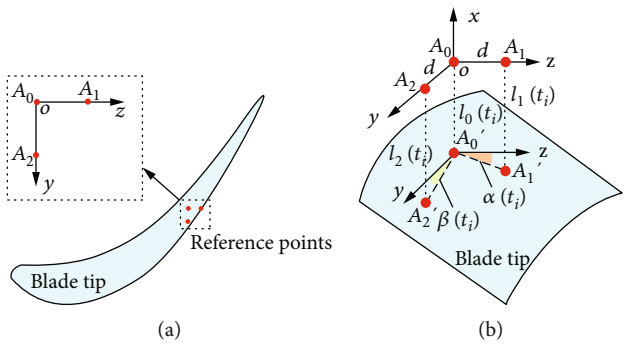

Figure 3: Schematic of the computation of 3D-BTC. (a) Reference points. (b) Schematic of the 3D-BTC computation.

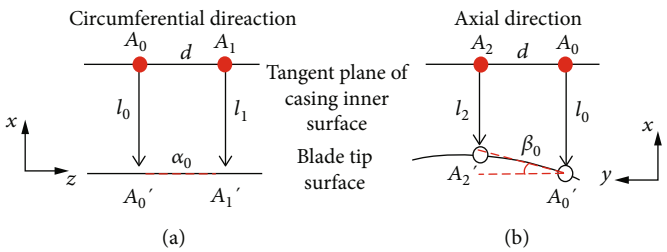

Figure 4: Schematic of the initial values of α_0 and β_0. (a) Schematic of α_0. (b) Schematic of β_0.

$$\frac{\partial(\rho\omega)}{\partial t}+\nabla\cdot(\rho\mathbf{U}\omega)=\nabla\cdot\left[\left(\mu+\frac{\mu_t}{\sigma_{\omega3}}\right)\nabla\omega\right]+2(1-F_1)\rho\frac{1}{\sigma_{\omega2}\omega}\nabla k\nabla\omega+\frac{\alpha}{\upsilon_t}\overline{P_k}-\beta\rho\omega^2, \quad (6)$$

$$\upsilon_t=\frac{a_1k}{\max(a_1\omega, SF_2)}. \quad (7)$$

Here, k and ω represent the turbulent kinetic energy and the turbulent frequency, respectively. The μ_t refers to turbulence viscosity, which is equal to $\rho k/\omega$. $\overline{P_k}=\min(P_k, 10\beta'\rho\omega k)$, and P_k is the turbulence production due to viscous forces, which can be modeled as follows [36]:

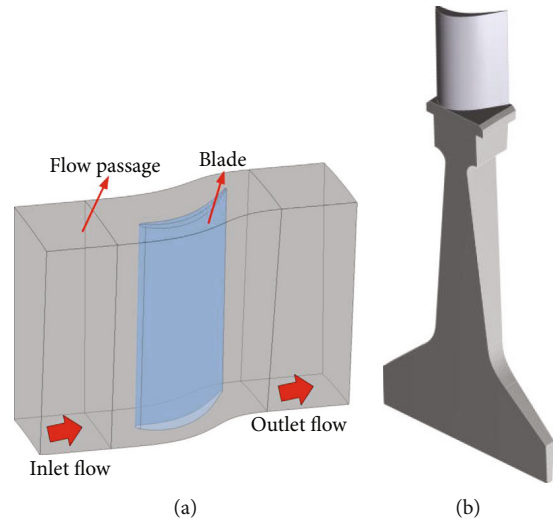

Figure 5: The geometric models. (a) The fluid flow model. (b) The turbine blisk model.

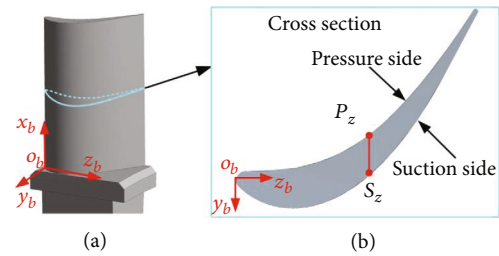

Figure 6: The schematic of crack position. (a) The position of blade cross-section. (b) The blade cross-section.

$$P_k=\mu_t\nabla\mathbf{U}\cdot\left(\nabla\mathbf{U}+\nabla\mathbf{U}^T\right)-\frac{2}{3}\nabla\cdot\mathbf{U}(3\mu_t\nabla\cdot\mathbf{U}+\rho k). \quad (8)$$

In the SST model, F_1 and F_2 refer to the blending functions, which are critical to the SST model and can be expressed as follows [36]:

$$F_1=\tanh\left(\arg_1^4\right),\quad \arg_1=\min\left[\max\left(\frac{\sqrt{k}}{\beta'\omega y},\frac{500\nu}{y^2\omega}\right),\frac{4\rho k}{CD_{k\omega}\sigma_{\omega2}y^2}\right],$$

$$F_2=\tanh\left(\arg_2^2\right),\quad \arg_2=\max\left(\frac{2\sqrt{k}}{\beta'\omega y},\frac{500\nu}{y^2\omega}\right), \quad (9)$$

$$CD_{k\omega}=\max\left(\frac{2\rho}{\sigma_{\omega2}\omega}\nabla k\nabla\omega, 1\times10^{-10}\right).$$

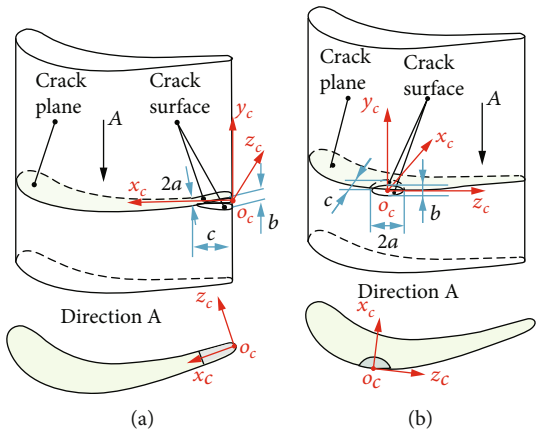

Figure 7: The schematic of crack size. (a) The through-thickness crack. (b) The surface crack.

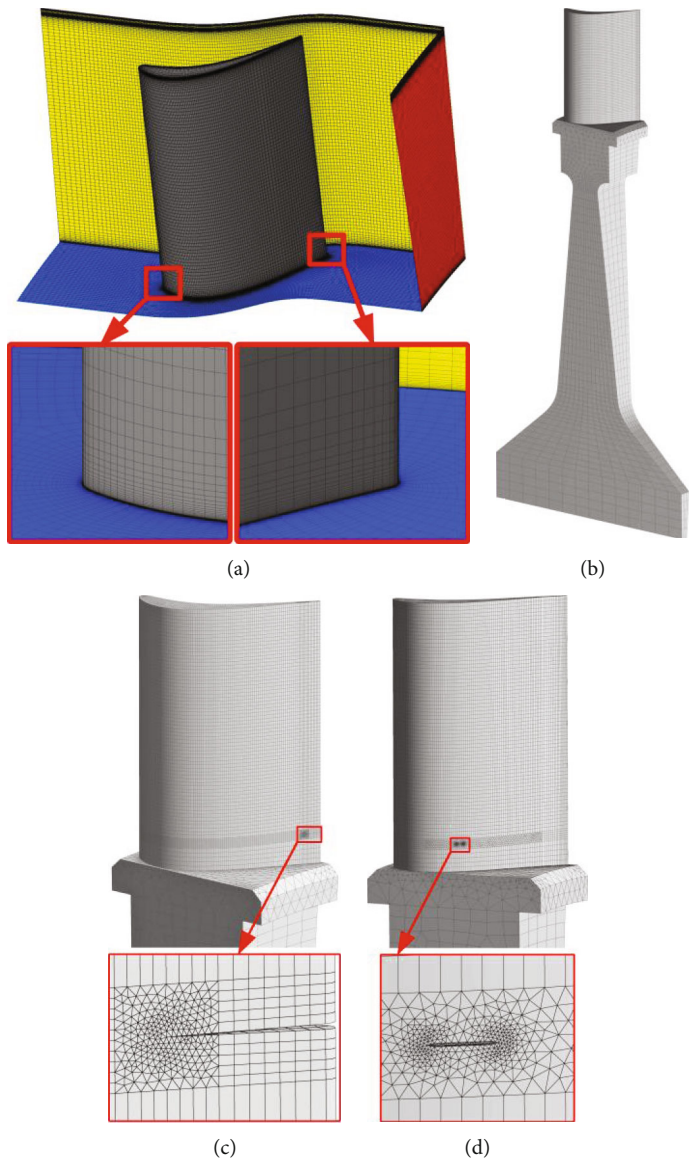

Figure 8: Computational mesh of the fluid passage and turbine blisk. (a) Mesh of the fluid passage. (b) Mesh of the turbine blisk. (c) Mesh of the cracked blade with the surface crack at the suction side. (d) Mesh of the cracked blade with the through-thickness crack at the trailing edge.

Table 1: The heat transfer coefficient and its relative error on the blade surface.

No.	Node number	Heat transfer coefficient (W/(m^{2}K))	Relative error (%)
1	0.93×10^6	5510.34	—
2	1.22×10^6	5166.79	6.23
3	1.60×10^6	5097.84	1.33
4	2.10×10^6	5112.92	0.30
5	2.76×10^6	5135.25	0.44
6	3.61×10^6	5148.32	0.25

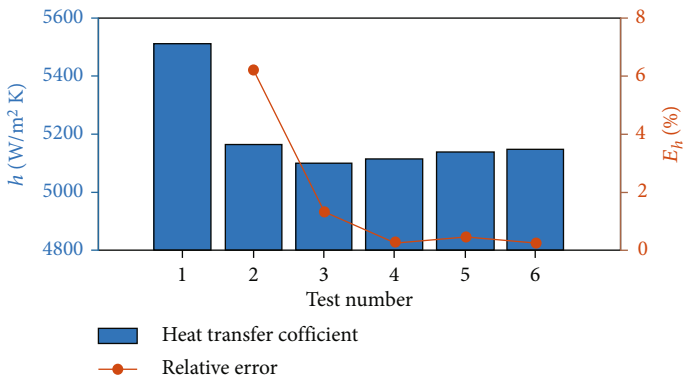

Figure 9: The results of the grid-independent test.

Here, y is the distance to the nearest wall, and ν is the kinematic viscosity. In Equations (5)–(7), α, β, β', $\sigma_{\omega 2}$, $\sigma_{\omega 3}$, and σ_{k3} are some constant coefficients. Through the fluid flow analysis, the temperature distribution and pressure distribution of the blade surface can be obtained.

The heat of the high-temperature gas will be transferred from the blade to the whole turbine disk. Thus, after the fluid flow analysis, the thermal analysis is implemented to obtain the temperature of the turbine blisk. As shown in Figure 2, the temperature distribution of the blade surface is transferred into the thermal analysis as the boundary condition. In the thermal analysis, Equation (10) is solved so that the temperature of the turbine blisk can be further obtained. Here, $\mathbf{K}_T$ is the conduction matrix, $\mathbf{T}$ is the temperature vector, and $\mathbf{Q}$ is the heat flow vector.

$$\mathbf{K}_T\mathbf{T} = \mathbf{Q}. \tag{10}$$

Then, the deformation of the turbine blade is obtained through structural analysis, as shown in Figure 2. In the structural analysis, the pressure distribution of the blade surface and the temperature of the turbine blisk are taken as the aerodynamic load and thermal load, respectively. The rotating speed of the turbine rotor is defined to apply the centrifugal load. The rotation angular displacement is also defined for the turbine rotor considering the operation of the turbine. Therefore, the dynamic equation of the structural analysis can be expressed as

Table 2: Material properties of GH4169.

Temperature (°C)	Young's modulus (GPa)	Poisson's ratio	Thermal expansion coefficient (10^{-6}/°C)
20	204	0.30	—
100	—	0.30	11.8
200	—	0.30	13.0
300	181	0.30	13.5
400	176	—	14.1
500	160	0.32	14.4
600	150	0.32	14.8
700	141	0.33	15.4

Table 3: Loads applied in the numerical simulation.

Load	Value
Inlet total temperature (K)	1400
Cooling air temperature (K)	700
Inlet total pressure (MPa)	3.60
Outlet static pressure (MPa)	2.16
Rotating speed (r/min)	8000
Rotation angular displacement (°)	6

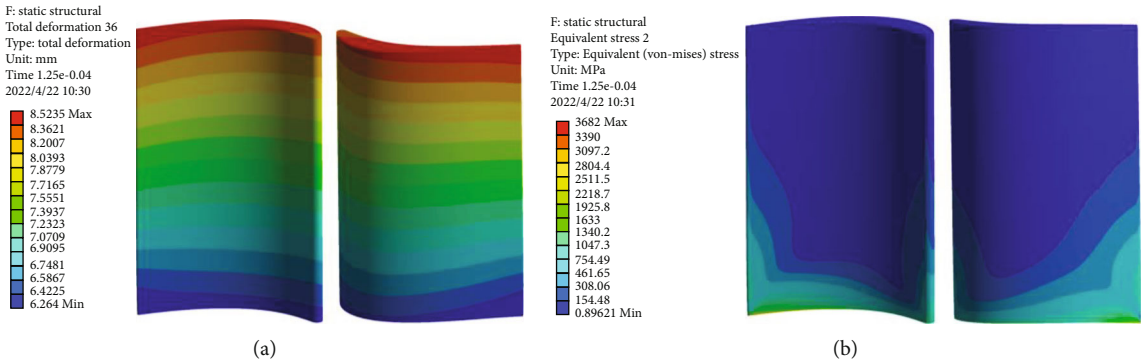

Figure 10: The contours of normal blades. (a) Deformation. (b) Stress.

$$\mathbf{M}\ddot{\mathbf{u}}(t) + \mathbf{C}\dot{\mathbf{u}}(t) + \mathbf{K}\mathbf{u}(t) = \mathbf{F}_a(t). \tag{11}$$

Here, **M**, **C**, and **K** are the structural mass matrix, damping matrix, and stiffness matrix, respectively. In addition, $\ddot{\mathbf{u}}(t)$, $\dot{\mathbf{u}}(t)$, and $\mathbf{u}(t)$refer to the acceleration vector, velocity vector, and displacement vector. The $\mathbf{F}_a$ is the applied load vector.

The fluid flow analysis, thermal analysis, and structural analysis are sequentially coupled, so it is important to ensure that the displacement, heat flow, temperature, and stress of the fluid and solid at the interface are equal. Therefore, the following conditions must be satisfied on the fluid-solid interface:

$$\begin{aligned} \mathbf{d}_f &= \mathbf{d}_s, \\ \mathbf{q}_f &= \mathbf{q}_s, \\ \mathbf{T}_f &= \mathbf{T}_s, \\ \mathbf{n}\cdot\boldsymbol{\tau}_f &= \mathbf{n}\cdot\boldsymbol{\tau}_s. \end{aligned} \tag{12}$$

Here, **d**, **q**, **T**, and $\boldsymbol{\tau}$ are the vectors of displacement, heat flow, temperature, and stress on the fluid-solid interface, respectively. The subscripts f and s represent fluid and solid, respectively. The **n** is the unit normal vector of the fluid-solid interface. The aforementioned sequential coupling analysis is implemented in the ANSYS Workbench software, and the deformation of the turbine blades can be obtained to calculate the 3D-BTC.

2.3. Dynamic Computation Method for the 3D-BTC. In this section, the dynamic computation method for the 3D-BTC is introduced. First of all, the reference points to calculate the 3D-BTC need to be determined. Since three parameters need to be calculated, at least three reference points are required. The 3D-BTC is measured by an optical fiber sensor with three sensing units arranged in an isosceles right triangle [21, 22], so three reference points (A_0, A_1, and A_2) are assumed to arrange in an isosceles right triangle, as shown in Figure 3(a). Besides, in order to determine the axial relative position between the reference points and the blade tip, the following factors are considered comprehensively. First, the reference points should be as close as possible to the crack so that the 3D-BTC can better reflect the crack fault of the turbine blade [24]. Second, the distances between the three reference points should be large enough to ensure the calculation accuracy of the 3D-BTC. Third, the blade tip should have sufficient thickness to ensure enough data can be extracted to analyze the dynamic characteristics of the 3D-BTC. Therefore, the axial locations of reference points are selected at the middle part of the blade tip, as shown in Figure 3(a).

In addition, the reference points should be located at the casing inner surface instead of the blade tip surface. Therefore, a coordinate system *oxyz* is established at the position of the initial radial clearance above the blade tip, and the *yoz* plane represents the inner surface of the casing. Thus, reference point A_0 is assumed to be the origin of the coordinate system *oxyz*, and the reference points A_1 and A_2 are located in the *yoz* plane, as shown in Figure 3(b).

Based on three reference points on the casing inner surface, a novel dynamic computation method for the 3D-BTC is proposed. The reference points are static, when the turbine blade passes below the reference points, the 3D-BTC can be calculated. As shown in Figure 3(b), assuming that at time t_i $(i = 1, 2, \cdots, n)$, the radial projection points of the reference points A_0, A_1, and A_2 are simultaneously located on the blade tip surface and can be expressed as $A_0{}'$, $A_1{}'$, and $A_2{}'$, respectively. The radial distances between A_0 and $A_0{}'$, A_1 and $A_1{}'$, and A_2 and $A_2{}'$ are expressed as $l_0(t_i)$, $l_1(t_i)$, and $l_2(t_i)$, respectively. According to the geometric relationship between the blade tip surface and casing inner surface, the RTC $r(t_i)$, ADA $\alpha(t_i)$, and CDA $\beta(t_i)$ can be calculated by Equation (13). Here, d refers to the distance of A_1 and A_2 from A_0. The α_0 and β_0 refer to the initial values of ADA and CDA, respectively.

$$\begin{cases} r(t_i) = l_0(t_i), \\ \alpha(t_i) = \arctan\left[\dfrac{l_1(t_i) - l_0(t_i)}{d}\right] - \alpha_0, \\ \beta(t_i) = \arctan\left[\dfrac{l_2(t_i) - l_0(t_i)}{d}\right] - \beta_0. \end{cases} \tag{13}$$

The initial values of ADA and CDA exist because the blade tip is usually a curved surface, which can keep the BTC consistent throughout the whole blade tip surface. After the reference points are selected, the initial values of

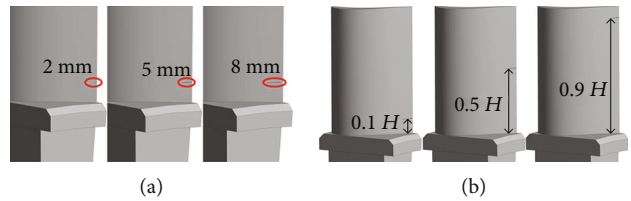

Figure 11: Turbine blades with through-thickness cracks. (a) The through-thickness cracks with different lengths. (b) The through-thickness crack with different positions.

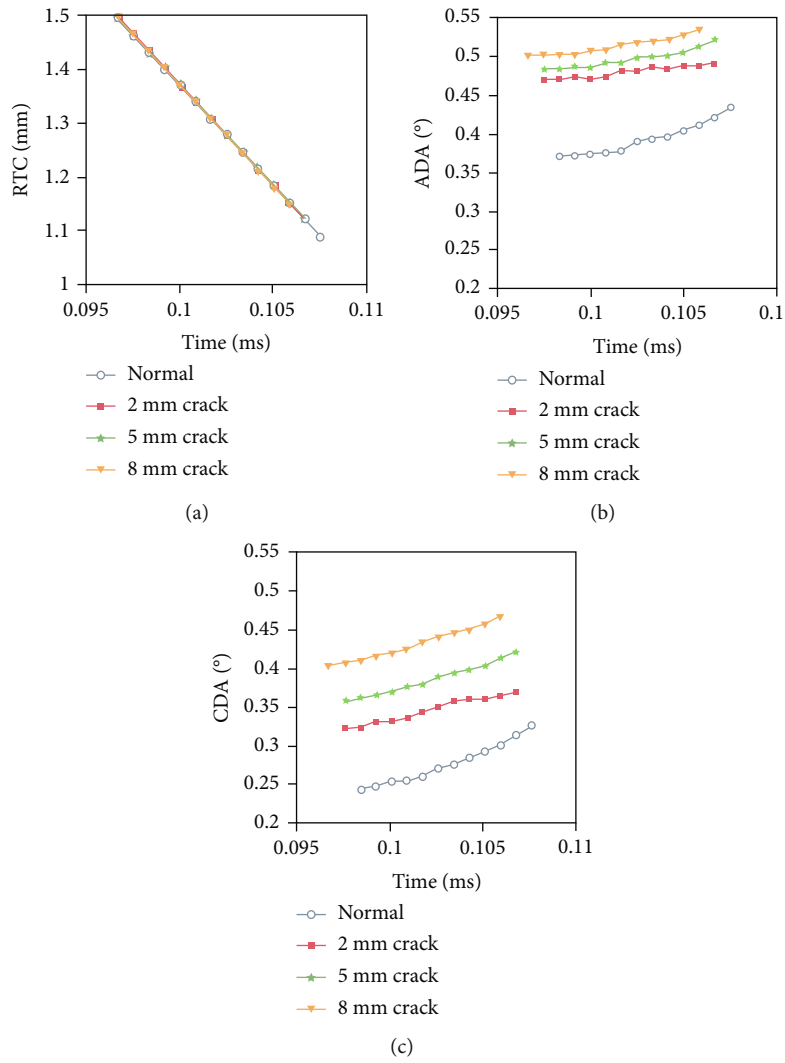

Figure 12: The 3D-BTC of blades with through-thickness crack of different depths. (a) RTC. (b)ADA. (c) CDA.

ADA and CDA can be determined, as shown in Figure 4. Assuming that the casing inner surface is cylindrical, the blade tip should be a cylindrical surface coaxial with the casing inner surface. Therefore, from the view of the circumferential direction of the turbine, the projection of the blade tip on the *xoz* plane can be regarded as a straight line, as shown in Figure 4(a). Thus, α_0 can be calculated by Equation (14), which is equal to 0° indeed. Meanwhile, from the view of the axial direction of the turbine, the projection of the blade tip on the *xoy* plane can be regarded as a circular arc, as shown in Figure 4(b). According to the geometrical relationship, β_0 can be calculated by Equation (14). The distances l_0, l_1, and l_2 can be easily calculated after the reference points are selected, and they are determined by the radius of the blade tip surface and the coordinate values of A_0, A_1, and A_2.

$$\begin{cases} \alpha_0 = \arctan \dfrac{l_1 - l_0}{d}, \\ \beta_0 = \arctan \dfrac{l_2 - l_0}{d}. \end{cases} \tag{14}$$

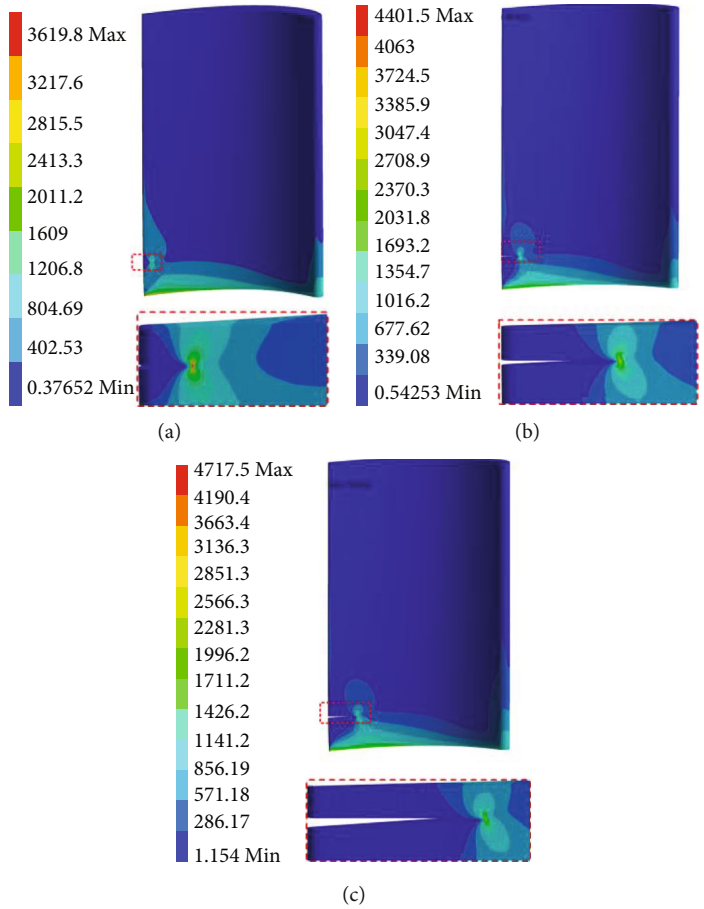

Figure 13: The stress distributions of blades with through-thickness cracks. (a) 2 mm. (b) 5 mm. (c) 8 mm.

The 3D-BTC can be calculated according to Equations (13) and (14), and the dynamic characteristics of the 3D-BTC can be further obtained. It should be noted that the 3D-BTC can be effectively calculated only when the projection points ($A_0{}'$, $A_1{}'$, and $A_2{}'$) are simultaneously located on the blade tip.

3. Numerical Model for the Turbine Blade with Cracks

3.1. Geometric Model of Turbine and Typical Cracks of Blade. Considering that modern aeroengines are constantly seeking higher thrust-weight ratios, the geometric model of the turbine is established based on the integral blade disk. Two geometric models are established in this paper. One is the fluid flow model used in the fluid flow analysis, as shown in Figure 5(a). A turbine blade and the flow passage around the blade are built in this model. The other is the geometric model of the turbine blisk used in both thermal analysis and structural analysis, as shown in Figure 5(b). The complete turbine blisk has 60 blades, but the sector part with only one blade is built due to the rotational symmetry structure of the turbine blisk. The cyclic symmetry boundary condition is applied so that the computational cost of the FEM can be reduced.

In order to investigate the effect of the typical blade cracks on the 3D-BTC, cracks need to be added to the model of the turbine blade. First, to describe the crack position, the coordinate system $o_b x_b y_b z_b$ is established at the leading edge of the blade root plane, as shown in Figure 6(a). Assuming that the crack is parallel to the blade tip surface, a blade cross-section can be selected as the crack plane, whose radial distance from the blade root plane is x_b. In the crack plane, the crack position can be determined by the axial coordinate z_b, as shown in Figure 6(b). When the axial position z_b is determined, the cracks can only appear in two positions. One is the P_z on the pressure side, and the other is the S_z on the suction side. Therefore, P_z and S_z are used to describe the crack on the pressure side and the suction side of the blade, respectively, and the subscript z represents the axial position of the crack. In this paper, the range of z_b is from 0 mm to 40 mm, so z_b equal to 0 mm and 40 mm means that the crack is located at the leading edge and trailing edge of the blade, respectively.

Both the through-thickness crack and the surface crack are considered in this paper, and the crack front of the through-thickness crack is straight, while that of the surface crack is usually semielliptical [27]. Thus, in order to describe the size of two cracks uniformly, the coordinate system $o_c x_c y_c z_c$ is established at the crack plane, as shown in Figure 7. The axes

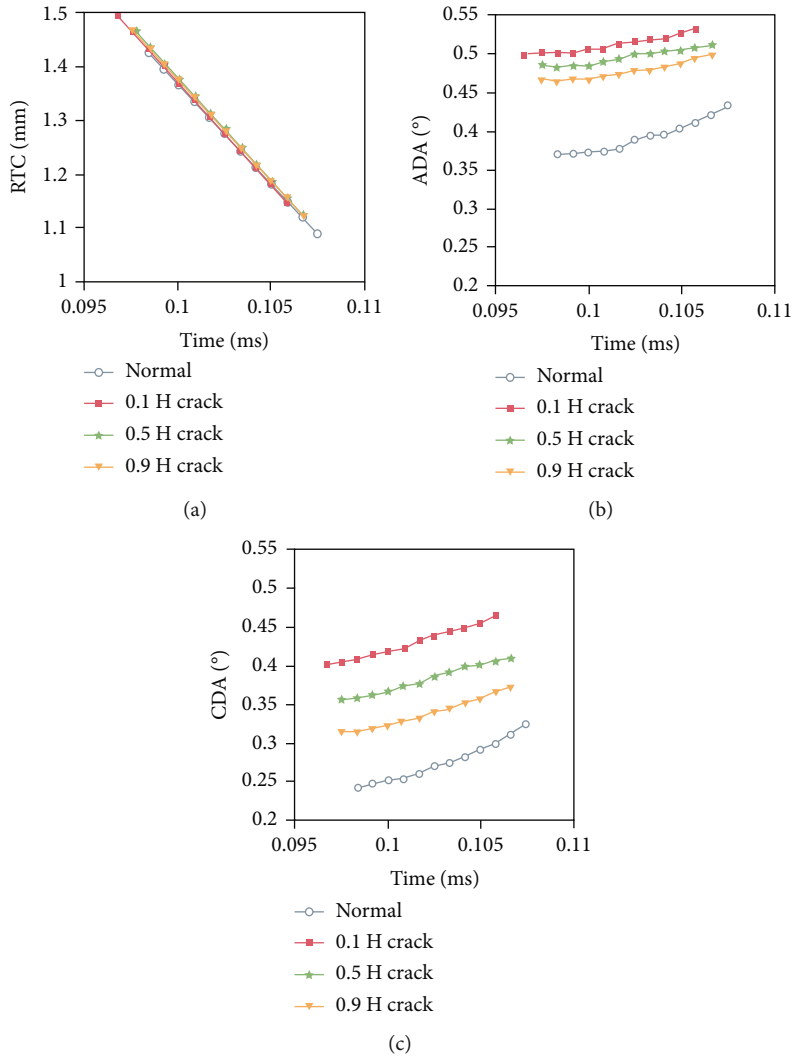

Figure 14: The 3D-BTC of blades with through-thickness cracks at different positions. (a) RTC. (b) ADA. (c) CDA.

x_c and z_c lie in the crack plane, and the axis y_c is perpendicular to the crack plane. The positive direction of x_c represents the growth direction of the crack, and the origin of the coordinate system is located at the crack initiation position. Therefore, the crack size can be described with the crack length $2a$, crack depth c, and crack opening width b. The schematics of the crack size for the through-thickness crack and surface crack are shown in Figures 7(a) and 7(b), respectively.

3.2. Mesh of Turbine Blisk and Cracked Blades. For the fluid flow model shown in Figure 5(a), the structured hexahedral mesh is generated for the computational domain, as shown in Figure 8(a). In order to accurately obtain the thermal and flow characteristics of the boundary layer between the blade and fluid, the grid is refined to ensure that $y+$ is equal to 1 within the boundary layers. Besides, the grid independence test is performed to ensure the reliability of the simulation results and determine the number of nodes. Six tests are performed with the node number increasing from 0.93 million to 3.61 million, as shown in Table 1. The area-averaged heat transfer coefficient h and its relative error E_h on the blade surface are calculated to determine the proper grid, which can be expressed as

$$h = q(T_w - T_a), \tag{15}$$

$$E_h = \frac{|h_{i+1} - h_i|}{h_i} \times 100\%. \tag{16}$$

Here, q is the heat flux of the wall surface, T_w is the constant wall temperature under isothermal boundary conditions, and T_a is the adiabatic wall temperature under adiabatic boundary conditions. The results of the grid-independent test are shown in Figure 9. It can be found that when the node number exceeds 2.1 million, the relative error is less than 1%, and the change is very small. Therefore, nearly 2.1 million nodes are generated for the fluid flow model.

As for the turbine blisk model shown in Figure 5(b), the tetrahedral mesh is generated at the rim of the disk due to its complex shape, and the hexahedral mesh is generated for the rest part of the turbine blisk to reduce the node number, as shown in Figure 8(b). Two typical cracks are added to the

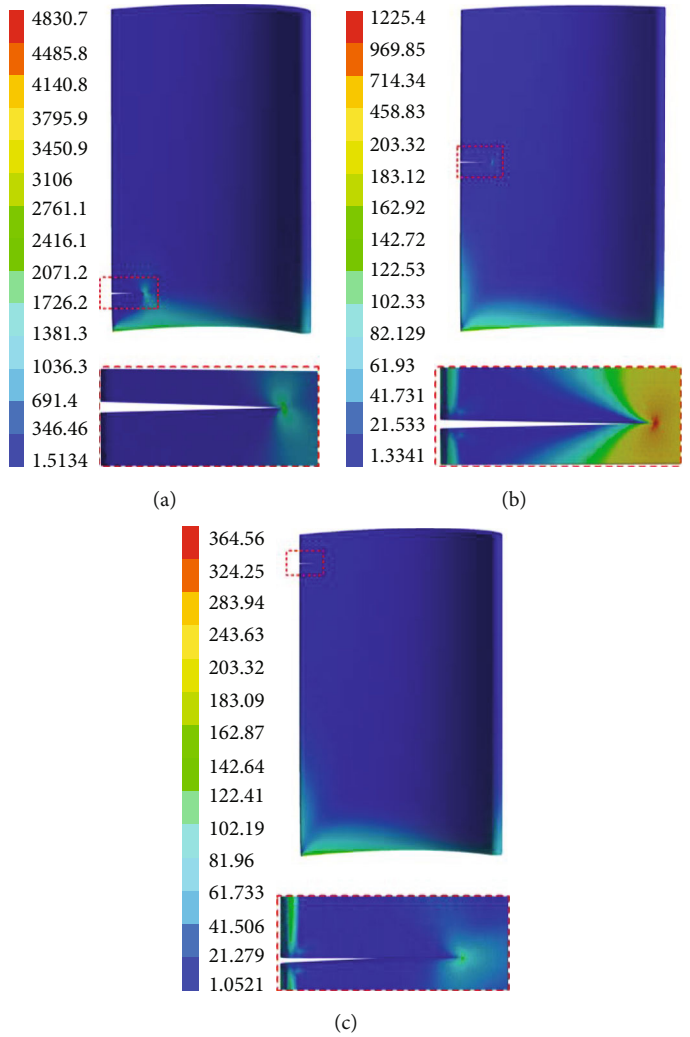

Figure 15: The stress distributions of blades with through-thickness cracks. (a) 0.1H. (b) 0.5H. (c) 0.9H.

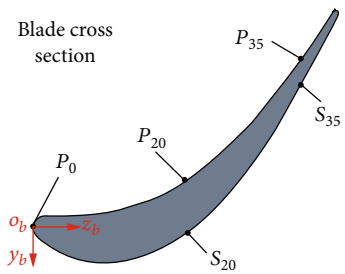

Figure 16: Different positions to add the surface cracks.

turbine blade, and the meshes of blades with the through-thickness crack and surface crack are shown in Figures 8(c) and 8(d). Because of the singularity of the stress field at the crack tip, the tetrahedral mesh is employed in the area around the crack front [37]. Besides, the mesh is further refined around the crack tip, and the hexahedral mesh is applied to the rest part of the cracked blade.

3.3. Material Properties, Loads, and Boundary Conditions. The turbine blisk is usually made of heat-resisting material due to its high-temperature working environment. Thus, the nickel-based superalloy GH4169 is used as the material of the blisk. The density of GH4169 is 8240 kg/m^3, and Young's modulus, Poisson's ratio, and thermal expansion coefficient depend on the temperature, which is listed in Table 2 [38].

The turbine is assumed to operate under steady-state conditions, and the loads and boundary conditions of the FE analysis are determined according to the typical working conditions of the turbine. In the fluid flow analysis, the inlet total temperature and total pressure of the turbine are 1400 K and 3.6 MPa, respectively, the outlet static pressure of the turbine is 2.16 MPa, and the rotating speed is 8000 r/min. The rotational periodic boundary conditions are applied on both lateral sides of the computational domain. In the thermal analysis, the temperature distribution of the blade surface is imported as the thermal boundary condition. Moreover, considering that the turbine disk is subjected to cooling air from the compressor, a constant temperature (700 K) is applied to the surface of the turbine disk. In the structural analysis, the pressure distribution of blade surface and the temperature of turbine blisk are imported as aerodynamic load and thermal load, respectively. The centrifugal load is simulated by

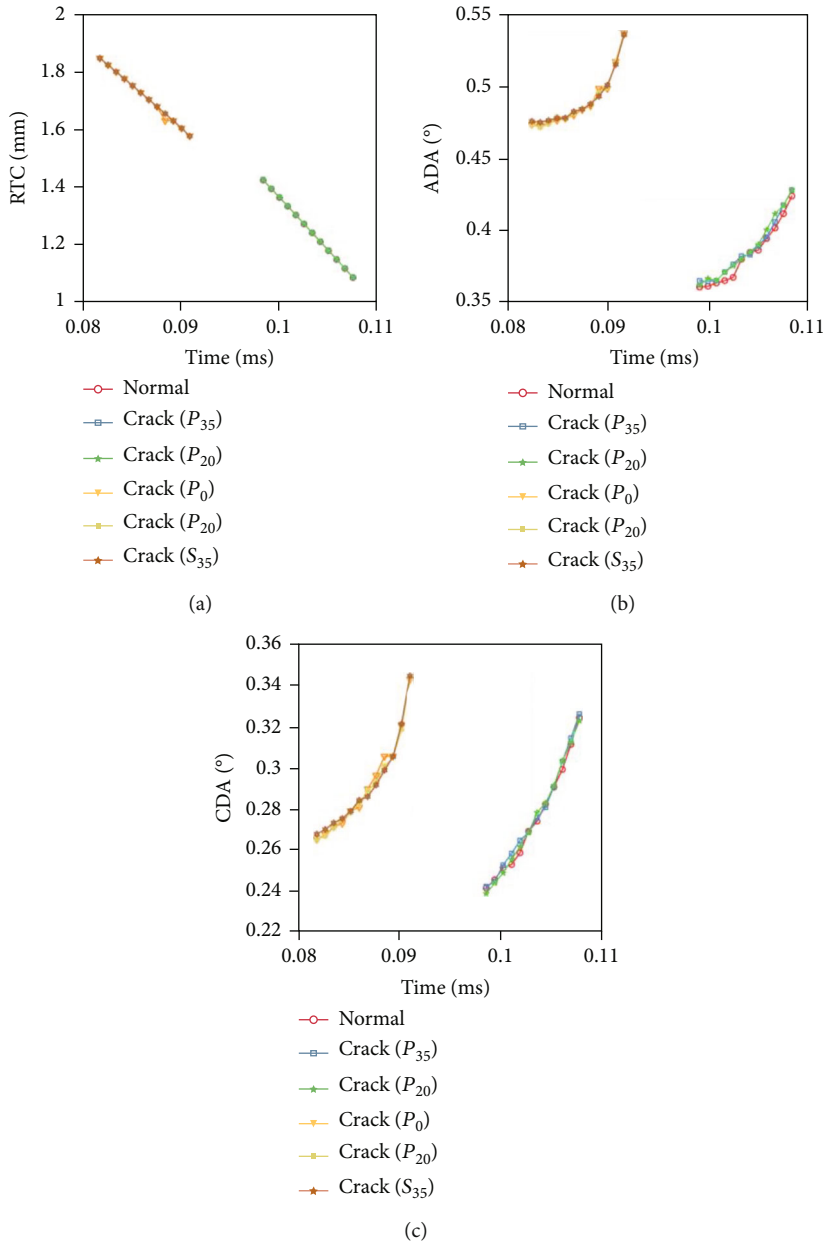

Figure 17: The 3D-BTC of blades with surface cracks of different positions. (a) RTC (b) ADA. (c) CDA.

applying the rotating speed of 8000 r/min. Because only a sector of the turbine blisk is modeled, the cyclic symmetry boundary condition is applied to the turbine disk. Besides, the rotation angular displacement of 6° is applied to the turbine, so the relative position change between the blade tip and reference points can be simulated, and the dynamic characteristics of the 3D-BTC can be further obtained. All loads applied in this paper are summarized in Table 3.

4. Dynamic Characteristics Analysis of the 3D-BTC of Cracked Blades

The FE analysis is performed on the normal blade at first so that the crack position can be better determined according to the FE analysis results. The deformation and stress contours of the normal blade are shown in Figure 10. It can be found that the maximal blade deformation appears at the blade tip while the maximal stress occurs at the blade root. The larger stress is more likely to lead to crack initiation, so the cracks are mainly located near the blade root in the following analysis. The through-thickness crack and surface crack are the most typical cracks of the turbine blades [27], so the 3D-BTC of blades with the through-thickness crack and surface crack is analyzed in this section.

4.1. 3D-BTC Dynamic Characteristics Analysis of Turbine Blades with Through-Thickness Cracks

4.1.1. Effect Analysis of Through-Thickness Crack Depth on the 3D-BTC. As shown in Figure 7(a), the crack size can be

described with three parameters. The crack length $2a$ of the through-thickness cracks is mainly determined by the blade thickness, and the crack opening width b is relatively small and usually changes little. Therefore, the effects of crack depth c on the 3D-BTC are analyzed. In this paper, the through-thickness crack with the crack depth of 2 mm, 5 mm, and 8 mm is investigated, and the crack opening width b is 0.1 mm, as shown in Figure 11(a). The through-thickness cracks usually appear in the position where the blade thickness is thin, so the crack position is selected at the trailing edge of the blade. Besides, according to the stress distribution of the normal blade, as shown in Figure 10(b), the crack plane is selected at the distance of $0.1H$ from the blade root plane, where H refers to the height of the blade.

The change rules of the 3D-BTC for different turbine blades are shown in Figure 12. It can be seen that the 3D-BTC is calculated only in a small period because the 3D-BTC can be effectively calculated only when the projection points are simultaneously located on the blade tip, as mentioned in Section 2.3. The 3D-BTC of the normal blade and cracked blades has an identical change trend, and the RTC is almost the same, as shown in Figure 12(a). The RTC is mainly affected by the radial deformation caused by the centrifugal load and thermal load. As the through-thickness crack will lead to the blade stiffness reduction, the radial deformation of the cracked blade under the centrifugal load will be larger than that of the normal blade. However, the effect of centrifugal load on the blade radial deformation is relatively small compared with that of the thermal load. Therefore, under the thermal load and centrifugal load, the normal blade and cracked blades have similar RTC.

The change rules of the ADA and CDA of different turbine blades are shown in Figures 12(b) and 12(c), respectively. It can be observed that both the ADA and CDA get larger with the increase of crack depth. The ADA and CDA are mainly affected by the bending deformation of turbine blades, and the blade bending stiffness is highly dependent on the crack fault. The blade with a deeper crack has a smaller bending stiffness, so the bending deformation of which is more obviously under identical bending loads. Therefore, the blade with a crack depth of 8 mm has the maximal ADA and CDA.

To better understand the effects of the through-thickness crack depth on the 3D-BTC, the stress distributions of different cracked blades are obtained based on the FE analysis, as shown in Figure 13. It can be found that the butterfly-shaped stress distribution zone appears at the crack front, and the stress near the crack front increases with the crack depth. Combined with Figure 12, the ADA and CDA not only increase with the crack depth but also reflect the increase of the stress near the crack front.

According to the change of the conventional RTC, it is really hard to distinguish the turbine blades with different crack depths. However, the fault information of blade crack depth can be obtained based on the 3D-BTC, which indicates that the 3D-BTC can provide more fault information on blade cracks.

4.1.2. Effect Analysis of Through-Thickness Crack Position on the 3D-BTC. The turbine blades with the through-thickness crack at different positions are shown in Figure 11(b). The distances between the crack plane and the blade root plane are $0.1H$, $0.5H$, and $0.9H$, respectively. The crack opening width b is 0.1 mm, and the crack depth c is 8 mm. The change rules of the 3D-BTC for cracked blades with different positions are shown in Figure 14.

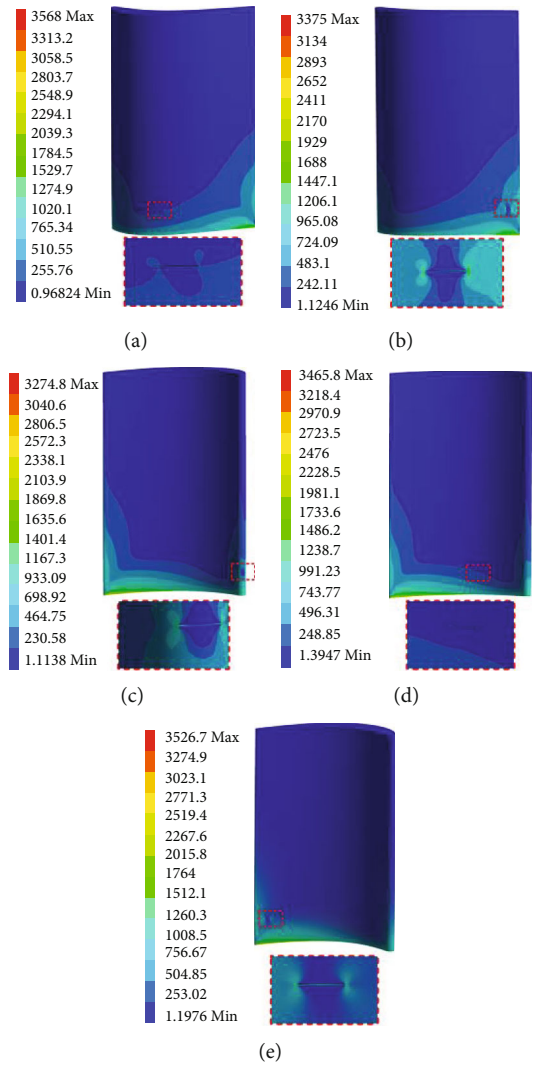

FIGURE 18: The stress distributions of blades with surface cracks. (a) S_{20}. (b) S_{35}. (c) P_0. (d) P_{20}. (e) P_{35}.

The RTC of blades with different crack positions is almost the same, as shown in Figure 14(a). As mentioned before, the radial deformation of the blade is dominated by the thermal load, so the position of the through-thickness crack has little effect on the RTC of blades. Moreover, combined with Figure 12(a), it can be found that the conventional RTC is insensitive to the depth and position of the through-thickness crack. However, the effects of the through-thickness crack position on the ADA and CDA can be observed, as shown in Figures 14(b) and 14(c). Both the ADA and CDA decrease gradually with the crack position away from the blade root. Thus, the blade with the through-thickness crack near the blade root has larger ADA and CDA. The ADA and CDA are mainly dependent

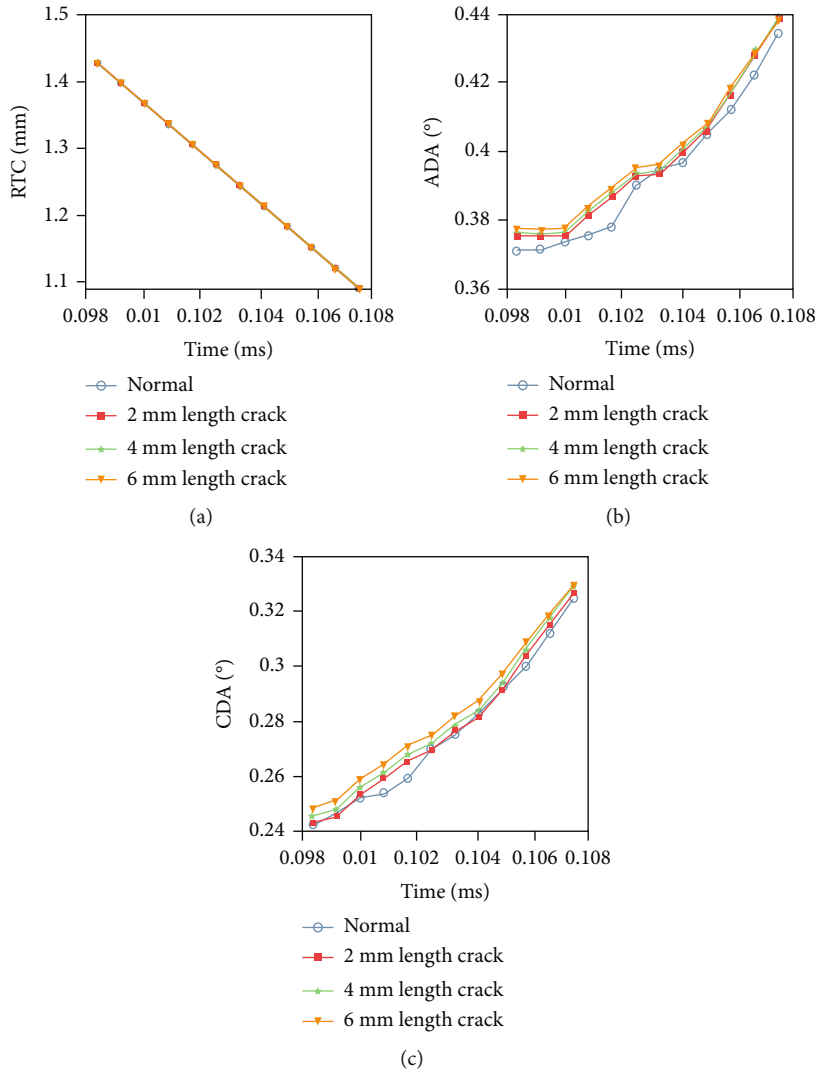

Figure 19: The 3D-BTC of blades with surface cracks of different lengths. (a) RTC (b) ADA. (c) CDA.

on the blade bending deformation caused by the aerodynamic load. The through-thickness crack near the blade root leads to the larger stiffness reduction of the blade, which further results in the larger blade bending deformation and larger ADA and CDA.

The stress distributions of blades with through-thickness cracks at different positions are also obtained based on the FE analysis, as shown in Figure 15. It can be found that the stress near the crack front decreases when the through-thickness crack position is away from the blade root. The variation trend of the stress near the crack front is coincident with that of the ADA and CDA. Therefore, the ADA and CDA can also reflect the stress change near the crack front at different positions.

Compared with the conventional BTC, the 3D-BTC can better reflect the fault information of turbine blades with through-thickness cracks. The information of the through-thickness crack depth and position can be reflected on the 3D-BTC, which is beneficial for the comprehensive fault diagnosis of blade cracks.

4.2. 3D-BTC Dynamic Characteristics Analysis of Turbine Blades with Surface Cracks

4.2.1. Effect Analysis of Surface Crack Positions on the 3D-BTC. According to the stress distribution of the normal blade, as shown in Figure 10(b), the stress near the blade root is larger, so the blade cross-section $0.1H$ away from the blade root is selected to add the surface cracks. Besides, the surface crack may appear at the leading edge, pressure side, and suction side of the turbine blade [27], so five positions are selected to add the surface crack to investigate the effects of surface crack position on the 3D-BTC, as shown in Figure 16. The position P_0 represents that the crack is located at the leading edge of the blade. The other four positions are selected at the areas with larger stress gradients according to Figure 10(b), and the subscripts 20 and 35 represent that z_b is 20 mm and 35 mm, respectively. The crack length $2a$ is 2 mm, the crack opening width b is 0.1 mm, and the crack depth c is 1 mm. The change rules of the 3D-BTC for turbine blades with surface cracks of different positions are shown in Figure 17.

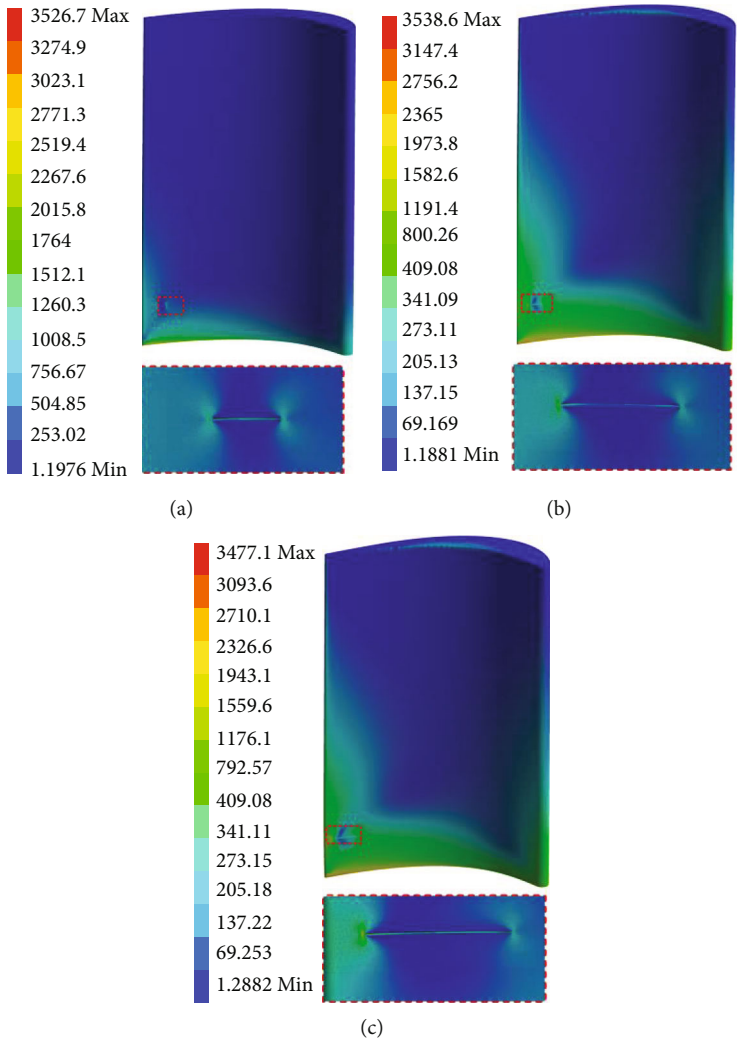

Figure 20: The stress distributions of blades with surface cracks. (a) 2 mm. (b) 4 mm. (c) 6 mm.

According to Figure 17, the 3D-BTC of the blades with surface cracks on the pressure side (P_{20} and P_{35}) is almost the same as that of the normal blade. Because the surface crack does not penetrate the thickness of the blade, its effects on the blade stiffness reduction are relatively small compared with the through-thickness crack. Besides, the crack size is quite small in this paper. Therefore, the surface cracks on the pressure side of the blade have limited effects on the 3D-BTC, which also indicates that the 3D-BTC is insensitive to the surface crack with a small size on the pressure side. Moreover, the stress distributions of blades with surface cracks at P_{20} and P_{35} are obtained, as shown in Figures 18(d) and 18(e). Compared with the stress distribution of the normal blade, as shown in Figure 10(b), it can be observed that the surface cracks at P_{20} and P_{35} have little effect on the stress distribution of the blade, so their effects on the 3D-BTC are also unobvious.

It can be seen from Figure 17 that the 3D-BTC of the blades with the surface crack at S_{20}, S_{35}, and P_0 is coincident with each other. However, the 3D-BTC of these blades can be distinguished from that of the normal blade. Under the direct impact of the aerodynamic load, the direction of blade bending deformation is from the pressure side to the suction side. When there is a surface crack on the suction side or leading edge of the blade, the bending deformation of the blade is more prominent and further results in the larger 3D-BTC. Besides, the stress distributions of blades with surface cracks at S_{20}, S_{35}, and P_0 are shown in Figures 18(a)–18(c), respectively. The butterfly-shaped stress distribution zone can be observed near the crack front, so the 3D-BTC of blades with surface cracks at S_{20}, S_{35}, and P_0 can be distinguished from the normal blade.

The surface crack is relatively weak compared with the through-thickness crack because it does not penetrate the blade, so the surface crack has weaker effects on the 3D-BTC. Therefore, the 3D-BTC is insensitive to surface cracks at different positions, but the blade with surface cracks on the suction side and leading edge can be preliminarily distinguished from the normal blade based on the 3D-BTC.

4.2.2. Effect Analysis of Surface Crack Length on the 3D-BTC. As for the surface crack, the crack length $2a$ can be directly observed, as shown in Figure 7(b), so it is more intuitive to

describe the severity of the surface crack by the crack length instead of the crack depth. Therefore, the effects of surface crack length on the 3D-BTC are investigated. Besides, considering that the surface cracks are relatively weak, the position P_{35} is selected to add surface cracks of different lengths because the blade thickness is thinner at P_{35}. The crack plane is $0.1H$ from the blade root. The surface cracks with lengths of 2 mm, 4 mm, and 6 mm are added to the blade, and the crack opening width b is 0.1 mm, and the crack depth c is 1 mm. The change rules of the 3D-BTC for turbine blades with surface cracks of different lengths at the position P_{35} are shown in Figure 19.

It can be found that with the increase of the surface crack length, the RTC remains unchanged, while the ADA and CDA increase slightly. As aforementioned, the surface crack does not penetrate the blade, so its effects on the blade stiffness reduction are much less than the through-thickness cracks. Therefore, the effects of the surface crack length on the 3D-BTC are relatively small compared with that of the through-thickness crack. Nevertheless, the blades with different surface crack lengths can still be better distinguished based on the 3D-BTC compared with the conventional RTC. Besides, the stress distributions of blades with surface cracks of different lengths are shown in Figure 20. With the increase of the surface crack length, the stress near the crack front increases slightly, which also indicates that the surface crack length only has slight effects on the 3D-BTC.

According to the above analysis, the 3D-BTC can reflect the severity of two typical cracks and the position of the through-thickness crack. Besides, the position of the surface crack on the leading edge and suction side of the blade also can be preliminarily distinguished from the normal blade based on the 3D-BTC. Therefore, the 3D-BTC is a better blade crack fault information carrier compared with the conventional RTC.

5. Conclusions

In this paper, a novel dynamic computation method is proposed to calculate the 3D-BTC based on the reference points on the casing inner surface and the blade deformation obtained from the FEM. The stress field nearing the crack front and the dynamic characteristics of the 3D-BTC regarding the typical cracks are obtained, and the effects of crack position and crack size on the 3D-BTC are analyzed. As for the through-thickness crack, the ADA and CDA of cracked blades increase with the through-thickness crack depth and decrease gradually when the through-thickness crack is away from the blade root, while the RTC of cracked blades is insensitive to the through-thickness cracks. Besides, the ADA and CDA can reflect the stress near the crack front. The effects of the surface crack on the 3D-BTC are relatively small compared with the through-thickness crack because the surface crack does not penetrate the blade, so it has little effect on the blade stiffness reduction. The blades with surface cracks on the suction side and the leading edge can be preliminarily distinguished from the normal blade based on the 3D-BTC. Moreover, the ADA and CDA increase slightly with the surface crack length despite the weak surface crack. Compared with the conventional RTC, the 3D-BTC contains more useful fault information about the position and size of turbine blades with typical cracks, which can be utilized to facilitate the comprehensive diagnosis of turbine blade cracks.

Data Availability

The data used to support the findings of this study are included in the article.

Conflicts of Interest

The authors declare that there is no conflict of interest regarding the publication of this paper.

Acknowledgments

The research was supported by the National Natural Science Foundation of China (Grant no. 52175117).

References

[1] Y. Chiu and S. Huang, "The influence of a cracked blade on rotor's free vibration," *Journal of Vibration and Acoustics*, vol. 130, no. 5, p. 54502, 2008.

[2] I. Y. Zablotskiy and Y. A. Korostelev, *Measurement of Resonance Vibrations of Turbine Blades with the ELURA Device*, Foreign Technology Div Wright-Patterson AFB OH, Technology Report, 1978.

[3] S. Heath and M. Imregun, "An improved single-parameter tip-timing method for turbomachinery blade vibration measurements using optical laser probes," *International Journal of Mechanical Sciences*, vol. 38, no. 10, pp. 1047–1058, 1996.

[4] S. Heath, "A new technique for identifying synchronous resonances using tip-timing," *Journal of Engineering for Gas Turbines and Power*, vol. 122, no. 2, pp. 219–225, 2000.

[5] S. Wu, Z. Zhao, Z. Yang, S. Tian, L. Yang, and X. Chen, "Physical constraints fused equiangular tight frame method for blade tip timing sensor arrangement," *Measurement*, vol. 145, pp. 841–851, 2019.

[6] J. Lin, Z. Hu, Z. Chen, Y. Yang, and H. Xu, "Sparse reconstruction of blade tip-timing signals for multi-mode blade vibration monitoring," *Mechanical Systems and Signal Processing*, vol. 81, pp. 250–258, 2016.

[7] Z. Wang, Z. Yang, S. Wu, H. Li, S. Tian, and X. Chen, "An improved multiple signal classification for nonuniform sampling in blade tip timing," *IEEE Transactions on Instrumentation and Measurement*, vol. 69, no. 10, pp. 7941–7952, 2020.

[8] Z. Xu, W. Zhu, G. Yi, and W. Fan, "Dynamic modeling and output error analysis of an imperfect hemispherical shell resonator," *Journal of Sound and Vibration*, vol. 498, article 115964, 2021.

[9] Z. Xu, G. Yi, and W. Zhu, "An accurate thermoelastic model and thermal output error analysis of a hemispherical resonator gyroscope under varying temperatures," *Mechanical Systems and Signal Processing*, vol. 170, article 108760, 2022.

[10] F. Xie, H. Ma, C. Cui, and B. Wen, "Vibration response comparison of twisted shrouded blades using different impact models," *Journal of Sound and Vibration*, vol. 397, pp. 171–191, 2017.

[11] Y. Oh and H. H. Yoo, "Vibration analysis of a rotating pretwisted blade considering the coupling effects of stretching, bending, and torsion," *Journal of Sound and Vibration*, vol. 431, pp. 20–39, 2018.

[12] M. W. Wiseman and T. Guo, "An investigation of life extending control techniques for gas turbine engines," in *Proceedings of the 2001 American Control Conference*, pp. 3706-3707, Arlington, USA, 2001.

[13] J. A. Kypuros and K. J. Melcher, *A Reduced Model for Prediction of Thermal and Rotational Effects on Turbine Tip Clearance*, National Aeronautics and Space Administration, Glenn Research Center, Technology Report, 2003.

[14] H. Agarwal, S. Akkaram, S. Shetye, and A. McCallum, "Reduced order clearance models for gas turbine applications," in *Proceedings of the 49th AIAA/ASME/ASCE/ AHS/ASC Structures, Structural Dynamics, and Materials Conference*, pp. 2008–2177, Schaumburg, USA, 2008.

[15] J. W. Chapman, J. Kratz, T. Guo, and J. Litt, "Integrated turbine tip clearance and gas turbine engine simulation," in *Proceedings of the 52nd AIAA/SAE/ASEE Joint Propulsion Conference*, pp. 2016–5047, Salt Lake City, USA, 2016.

[16] B. Jia, Y. Feng, G. Yan, and J. Zhang, "The influence of rotor crack on dynamic changes rule of turbine tip clearance," *Journal of Vibration, Measurement & Diagnosis*, vol. 36, no. 6, pp. 1153–1160, 2016.

[17] B. Jia and X. Zhang, "Study on effect of rotor vibration on tip clearance variation and fast active control of tip clearance," *Advanced Materials Research*, vol. 139–141, pp. 2469–2472, 2010.

[18] Y. Ju, "Research on turbine blade tip clearance test and numerical analysis," *Master dissertation*, Nanjing University of Aeronautics and Astronautics, 2016.

[19] F. Teng, X. Zhang, and S. Xie, "Research on variation mechanism of three-dimensional blade tip clearance of aero-engine," in *Proceedings of the 13th International Conference on Ubiquitous Robots and Ambient Intelligence (URAI)*, pp. 1–6, Xi'an, China, 2016.

[20] S. Xie, X. Zhang, B. Wu, and Y. Xiong, "Output characteristics of two-circle coaxial optical fiber bundle with regard to three-dimensional tip clearance," *Optics Express*, vol. 26, no. 19, pp. 25244–25256, 2018.

[21] S. Xie, X. Zhang, Y. Xiong, and H. Liu, "Demodulation technique for 3-D tip clearance measurements based on output signals from optical fiber probe with three two-circle coaxial optical fiber bundles," *Optics Express*, vol. 27, no. 9, pp. 12600–12615, 2019.

[22] X. Zhang, Y. Xiong, S. Xie, and H. Liu, "Optical-fiber-based dynamic measurement system for 3D tip clearance of rotating blades," *Optics Express*, vol. 27, no. 22, pp. 32075–32095, 2019.

[23] H. Liu, X. Zhang, Y. Xiong, and S. Xie, "Demodulating of the 3-D tip clearance of turbine blades using BP neural network optimized by genetic algorithm," in *Proceedings of Surveillance, VISHNO and AVE Conference*, Lyon, France, 2019.

[24] Y. Xiong, X. Zhang, S. Xie, and H. Liu, "Research on the variation mechanism of the 3-D tip clearance of a cracked blade under multi-parameters in the aero-engine acceleration process," in *Proceedings of Surveillance, VISHNO and AVE Conference*, Lyon, France, 2019.

[25] C. Liu, X. Yue, J. Zhang, and K. Shi, "Active disturbance rejection control for delayed electromagnetic docking of spacecraft in elliptical orbits," *IEEE Transactions on Aerospace and Electronic Systems*, vol. 58, no. 3, pp. 2257–2268, 2021.

[26] K. Shi, C. Liu, Z. Sun, and X. Yue, "Coupled orbit-attitude dynamics and trajectory tracking control for spacecraft electromagnetic docking," *Applied Mathematical Modelling*, vol. 101, pp. 553–572, 2022.

[27] H. Liu, X. Yang, S. Li, and D. Shi, "A numerical approach to simulate 3D crack propagation in turbine blades," *International Journal of Mechanical Sciences*, vol. 171, article 105408, 2020.

[28] M. Kianicova and J. Pokluda, "Fatigue fracture of turbine blades: case studies," *Key Engineering Materials*, vol. 592-593, pp. 712–715, 2013.

[29] Z. Chen and J. Chen, "The fracture analysis of turbine rotor blade," in *Proceedings of the 2nd International Conference on Energy and Power Engineering*, pp. 238–241, Chengdu, China, 2018.

[30] S. Kim, Y. Hwang, T. Kim, and C. Shu, "Failure analysis of J85 engine turbine blades," *Engineering Failure Analysis*, vol. 15, no. 4, pp. 394–400, 2008.

[31] A. Mokaberi, R. D. Haghighi, and Y. Abbaszdeh, "Fatigue fracture analysis of gas turbine compressor blades," *Engineering Failure Analysis*, vol. 58, pp. 1–7, 2015.

[32] K. Song, S. Kim, D. Jung, and Y. Hwang, "Analysis of the fracture of a turbine blade on a turbojet engine," *Engineering Failure Analysis*, vol. 14, no. 5, pp. 877–883, 2007.

[33] S. Qu, C. M. Fu, C. Dong, J. F. Tian, and Z. F. Zhang, "Failure analysis of the 1st stage blades in gas turbine engine," *Engineering Failure Analysis*, vol. 32, pp. 292–303, 2013.

[34] R. Ghorbani, S. Asadikouhanjani, K. Kusterer, and A. H. Ayed, "Fracture analysis of a first stage turbine blade," in *Proceedings of ASME Turbo Expo 2010: Power for Land, Sea and Air*, pp. 549–555, Glasgow, Scotland, 2010.

[35] H. Zhu, *Practical Guide to Thermal-fluid-Solid Coupling for ANSYS 14.5*, Posts and Telecom Press, 2014.

[36] L. Xie and X. Zhao, *Fluid Analysis and Simulation Based on ANSYS CFX*, Publishing House of Electronics Industry, 2013.

[37] H. Okada, H. Kawai, and K. Araki, "A virtual crack closure-integral method (VCCM) to compute the energy release rates and stress intensity factors based on quadratic tetrahedral finite elements," *Engineering Fracture Mechanics*, vol. 75, no. 15, pp. 4466–4485, 2008.

[38] Editorial board of China Aeronautical Materials Handbook, *China Aeronautical Materials Handbook*, vol. 2, Standards Press of China, 2002.